sustainability

MDPI

Article

Field Measurement and Mechanism Analysis of Rail Corrugation on Steel Spring Floating Slab Track Section

Kuikui Ma [1,2]

[1] Shanghai Key Laboratory of Rail Infrastructure Durability and System Safety, Tongji University, Shanghai 201804, China; makuikui@tongji.edu.cn
[2] The Key Laboratory of Road and Traffic Engineering, Ministry of Education, Tongji University, Shanghai 201804, China

Abstract: In this study, a combination method of field measurements and numerical simulations is used to investigate the mechanism of rail corrugation in the curve's inner rail in urban rail transit. Firstly, field measurements on rail corrugation and rail vibration characteristics were conducted on the steel spring floating slab track (SSFST) section of a metro line; secondly, a three-dimensional finite element model of the wheelset-SSFST was established, and complex eigenvalue analysis and transient analysis were conducted. It was found that the main frequency of measured rail vertical vibration and the simulated wheel–rail—which simulated normal contact force on the inner rail—correspond to the first wheel–rail unstable vibration mode, as well as to the field-measured rail corrugation passing frequency. Therefore, the strong agreement between the results of the field measurements and the numerical simulation further verifies that the frictional, self-excited vibration of the wheelset-SSFST system on a sharply curved track can cause rail corrugation. When the vertical and lateral fasteners' stiffness increases, the possibility of rail corrugation decreases. The decrease in vertical stiffness of the steel spring leads to an increase in the possibility of rail corrugation, but the lateral stiffness changes in the steel spring have almost no effect on the possibility of rail corrugation. The increase in the wheel–rail contact friction coefficient leads to a sharp increase in the trend of rail corrugation occurrence and causes a decrease in the rail corrugation wave-length.

Keywords: metro; steel spring floating slab track; rail corrugation; friction-induced oscillation; field measurement; numerical simulation

Citation: Ma, K. Field Measurement and Mechanism Analysis of Rail Corrugation on Steel Spring Floating Slab Track Section. *Sustainability* **2022**, *14*, 11790. https://doi.org/10.3390/su141811790

Academic Editor: Marinella Silvana Giunta

Received: 31 July 2022
Accepted: 15 September 2022
Published: 19 September 2022

1. Introduction

Rail corrugation refers to periodic, uneven wearing on a rail surface after a period of operation. It is a type of rail damage commonly found in world rail transportation [1]. Rail corrugation as the periodic unevenness of the rail surface intensifies the wheel–rail interaction, triggers the strong vibration of vehicles and tracks [2], rail fastener clip fracture, bogie cracking, and increases wheel–rail noise [3]. The strong interaction of the wheel and rail caused by rail corrugation makes the cracks (surface microcracks) that appear in the rail manufacturing process further expand [4]. At present, in order to deal with rail corrugation the rail must be regularly grinded; rail grinding does, however, contribute to crack formation [5]. Therefore, rail corrugation not only increases the maintenance cost of rail transit, and reduces the comfort of passengers, but also directly threatens operational safety.

Since 1889, when the phenomenon of rail corrugation was first recorded on the Midland line in England [6], scholars from various countries, now for more than one hundred years, have studied formation mechanisms and the characteristics of rail corrugation, as well as countermeasures for it [7]. Understanding the formation mechanism of rail corrugation comprises the premise of understanding and countering rail corrugation. The most-recognized mechanisms are the wavelength fixing mechanism and the damage mechanism. S. L. Grassie divided rail corrugation into six categories according to different and

fixed wavelength and damage mechanisms: pinned–pinned resonance ('roaring rails'), rutting, other P2 resonances, heavy haul, light rail, and rail track form specific [8]. Akira Matsumoto et al. [9] found that rail corrugation on curved tracks is mainly caused by the stick-slip vibration between the wheel–rail, and this was determined via full-scale stand tests, in situ measurements, and numerical simulation. Y. Q. SUN and Simson S. [10] also proved that the stick-slip vibration between the wheel–rail causes rail corrugation on heavy-haul railways by using a nonlinear three-dimensional wagon–track model. Rail corrugation occurs not only on curved tracks, but also on tangent tracks. K.H. Oostermeijer [11] discussed the observation results, mechanism, and control measures of rail corrugation with short-pitch studies on a straight line. Based on the wheelset–track resonance theory, Chaozhi Ma et al. [12] found that third-order bending of rails (the pinned–pinned resonance of rails between bogies), and second antisymmetric bending resonance of wheelsets, are the key factors to induce rail corrugation. They achieved this by establishing a multi-flexible wheelset–rail interaction model and including the W-TF (wave transmissions and reflections) effect. Thus, we see that the mechanism of rail corrugation is complex and there are many influencing factors. Further, as they are related to each part of the whole vehicle–track structure system, there is no unified mechanism to explain various rail corrugation phenomena [13]. It is necessary to integrate the vehicle, line, track, wheel–rail interaction, and other aspects to study the key influencing factors that induce rail corrugation.

There are a large number of curved tracks in the metro and many observations about them have been made. Rail corrugation is common in tightly curved tracks, especially in sections which have vibration-reduction tracks [14–16]. SSFST, as an effective vibration-reduction track structure, better counters train-induced environmental vibration effects [17], but the problem of rail corrugation on SSFST sections is also becoming more prominent. There are some studies that have focused on field observations [18] and their impacts on the wheel–rail system [19]. However, there are less studies on the mechanism of rail corrugation on the SSFST section, as well as the influence on the wheelset-SSFST coupling system parameters on rail corrugation.

To investigate the mechanism of rail corrugation and the influence of system parameters on SSFST sections, this paper firstly analyzes the typical wavelength of rail corrugation and rail vibration characteristics tested in the field. Secondly, using the frictional, self-excited vibration theory [20], a three-dimensional finite element model of the wheelset-SSFST is established, and the effective damping ratios—calculated by complex eigenvalue analysis—are used as an indicator to measure the stability of the wheelset-SSFST. The unstable mode of frictional, self-excited vibration is analyzed to study the causes of rail corrugation in this section. Thirdly, the rationality of using frictional, self-excited vibration theory to analyze the rail corrugation mechanism, in a sharp curved SSFST section of the metro, is verified by comparing the passing frequency and the system's unstable vibration characteristic frequency. Finally, the effects of the stiffness of fasteners, steel spring stiffness, and the wheel–rail friction coefficient on rail corrugation of the SSFST, are discussed.

2. Field Measurements

A field measurement interval was selected on the Suzhou Rail, Transit Line 2, which is an upstream line of Tongjing Park Station–Youlian Station. Since operation began, as shown in Figure 1a,b in the rail surface photos, rail corrugation of the SSFST section on this interval—especially on the inner rail—is more serious. After grinding the corrugation, as shown in Figure 1c, there is subsequently no rail corrugation on the inner rail surface. As shown in Figure 2 for the curve location, the curved test section mileage is K20 + 175~K20 + 564; the length is 389 m; the curve radius is 350 m; and the track structure is an SSFST—additionally, the fasteners are DTVI2 type fasteners. As shown in Figure 3, measurement equipment based on structured light [21] was used to measure the rail corrugation.

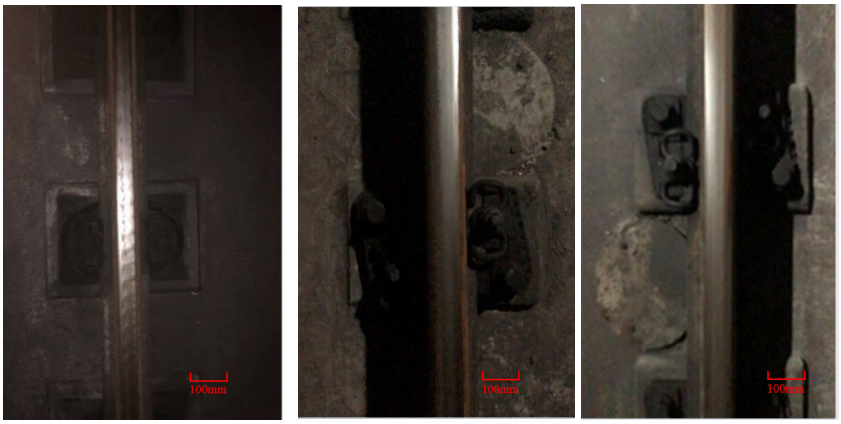

(**a**) (**b**) (**c**)

Figure 1. Photo of rail surface onsite: (**a**) inner rail; (**b**) outer rail; (**c**) inner rail surface after grinding.

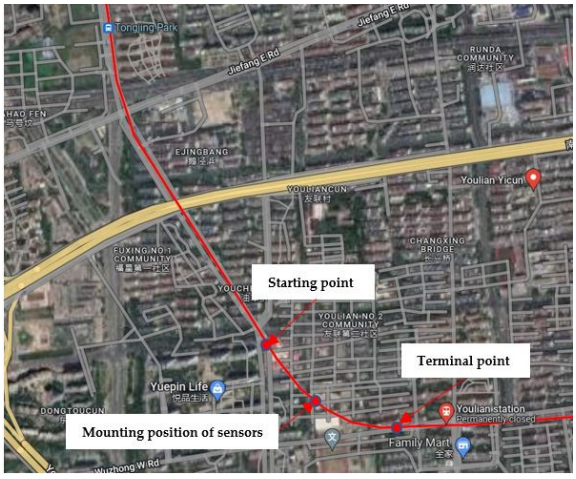

Figure 2. Measurement positions of the rail corrugation.

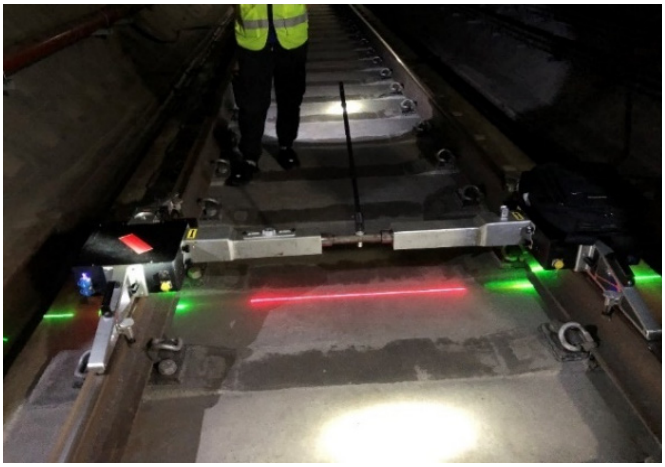

Figure 3. Rail corrugation measurement equipment.

To analyze the vibration response characteristics of rails when a vehicle passes through the SSFST, as shown in Figure 2 for the measurement position, field measurement of rail corrugation and rail vertical vibration was performed. Several vertical acceleration sensors were mounted at the mid-span position between two fasteners, as shown in Figure 4a. Further, as shown in Figure 4b, sensors were mounted on the bottom of the rail.

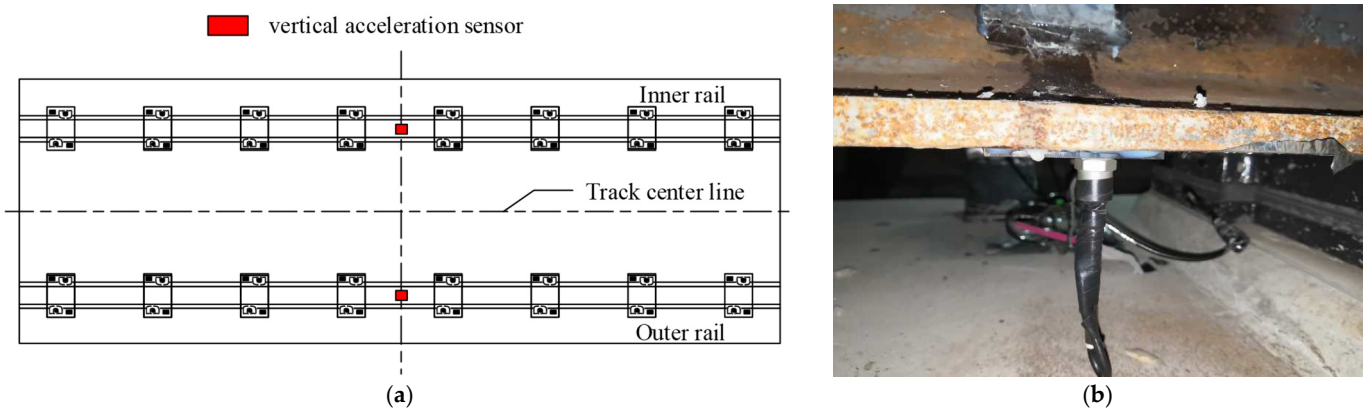

Figure 4. Mounting position of sensors on the rail: (**a**) mounting position of sensors on rails; (**b**) vertical acceleration sensors.

3. Numerical Simulation

3.1. Finite Element Model of the Wheelset-SSFST System

An SSFST system is composed of rails, fasteners, a floating slab, and steel springs. The wheelset runs on the track, and it is subjected to single-state suspension forces, as well as the interaction force between the wheel and rail, as shown in Figure 5. The length of the floating slab is 12.5 m, the thickness is 0.37 m, and the width is 2.7 m.

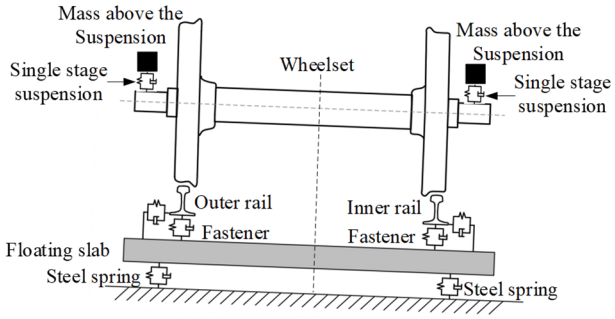

Figure 5. Schematic diagram of the wheelset-SSFST system.

The geometric dimensions of the wheelset are adopted from the B-type metro wheelset with LM wear-type tread, of which the mass is 1420 kg. The 7000 kg mass on each single-stage suspension is reduced and connected to the axle by a spring. The distance between fasteners is 0.625 m, and the distance between the steel springs is 1.85 m laterally and 1.25 m longitudinally.

As shown in Figure 6, the finite element model of the wheelset-SSFST system is established in the commercial, finite, element software ABAQUS, and is based on three-dimensional geometric shapes and the interaction of components. As shown in Figure 7a, the rail, wheelset, and floating slab entities are discretized by C3D4 elements and C3D8I elements, and the material parameters of the components in the model are listed in Table 1. The fasteners are simulated by discrete spring-damping elements and are connected to the corresponding nodes of the rail and the floating slab with a vertical stiffness of 40 KN/mm and lateral stiffness of 8.79 KN/mm, respectively. As shown in Figure 7b, the rail cant is set at 1:40. The wheel–rail contact behavior is simulated by the "face-to-face" contact algorithm based on the penalty function method. The friction coefficient is defined as 0.4. As shown in Figure 7c, the steel spring isolators are simulated by spring-damper elements and connected to the bottom of the floating slab, and ground, with a vertical stiffness of 5.3 KN/mm and lateral stiffness of 8 KN/mm, respectively. Further, the model has approximately 500,000 elements.

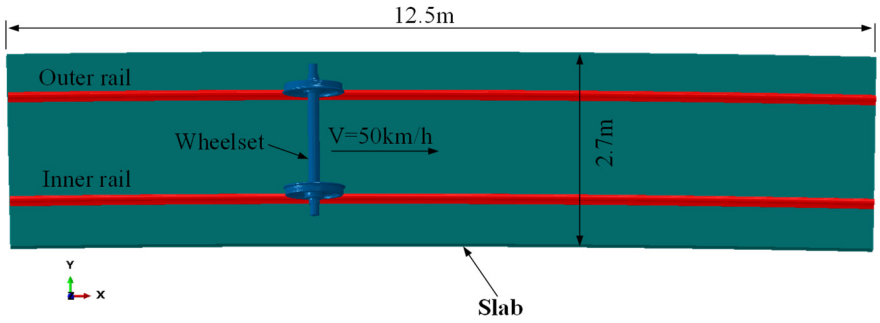

Figure 6. The overview of the model.

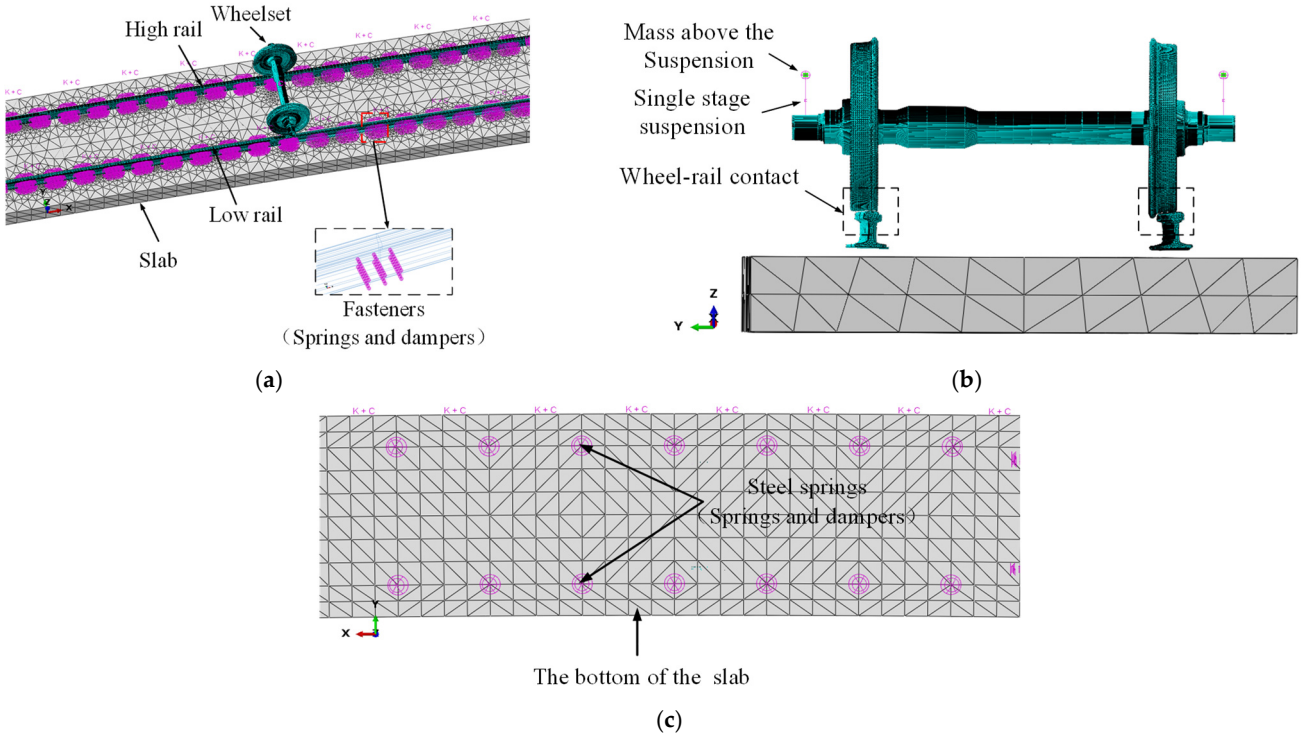

Figure 7. Finite Element Model of Wheelset-SSFST System: (**a**) the meshing of the 3D FEA model; (**b**) contact details between the wheels and rails; (**c**) steel spring distribution.

Table 1. Material Parameters of Wheelset-SSFST System.

Components	Density/(kg·m^{-3})	Young Modulus/Pa	Poisson's Ratio
wheelset	7800	2.1×10^{11}	0.3
rail	7790	2.059×10^{11}	0.3
Slab	2500	3.5×10^{10}	0.2

3.2. Analytical Methods

Based on the established model, the frictional, self-excited vibration frequencies and modes of the wheelset-SSFST system were first extracted using the complex eigenvalue analysis method [22], which was used to verify the formation mechanism of rail corrugation on the SSFST.

Then, transient dynamic analysis of the simulation model was carried out. The transient analysis was used to calculate the dynamic response of the system, in the time-

domain, when frictional, self-excited vibration occurs. The equations of motion for the wheelset-SSFST system can be written as [23]:

$$\mathbf{M}\ddot{x}_{(t)} = \mathbf{P}_{(t)} - \mathbf{I}_{(t)} \tag{1}$$

where **M** is the mass matrix of the system; x is the displacement of the node; **P** is the external force vector; **I** is the internal force vector of the system; and the subscript t is the time increment.

In the Abaqus/Implicit solver calculation of the implicit dynamics, the equations of motion (1) are integrated stepwise, using the Newmark method, which is integrated into the following format [24]:

$$\begin{cases} x_{(t+\Delta t)} = x_{(t)} + \Delta t\dot{x}_{(t)} + \Delta t^2(0.5-\beta)\ddot{x}_{(t)} + \beta\ddot{x}_{(t+\Delta t)} \\ \dot{x}_{(t+\Delta t)} = \dot{x}_{(t)} + \Delta t(1-\gamma)\ddot{x}_{(t)} + \gamma\ddot{x}_{(t+\Delta t)} \\ \beta = \left(1-\alpha^2\right)/4 \\ \gamma = 0.5-\alpha \end{cases} \tag{2}$$

where α is an intermediate variable, and $1/3 \leq \alpha \leq 0$.

When a metro vehicle passes through a small radius curve, the creep force on the left and right wheels of the guiding wheelset tends to saturate and—under certain conditions—the wheel–rail system will produce frictional, self-excited vibration, while the wheel–rail normal contact force will fluctuate with the same frequency [25]. During this stage, the value of the creep force F is approximately equal to the product of the normal contact force, between the wheels and the rails, and the coefficient of dynamic friction μ.

According to the wear equation proposed by Brockley, the wear of the rails can be derived from frictional work [26]:

$$w = K(H - C) \tag{3}$$

where w is the wear depth at a certain time; K is the wear coefficient; H is the friction power ($H = F \bullet v_r$, F is the friction force and v_r is the wheel–rail sliding speed); and C is the durability friction work rate.

Thus, frictional, self-excited vibration is a principal reason for the periodic wear of rails on small radius curves.

4. Results and Discussion

4.1. Measurement Results

With a longitudinal sampling interval of 5 mm, rail surface irregularity data in the range from K20 + 350 to K20 + 351 were extracted. The inner and outer rail surface irregularity values are shown in Figure 8. Before rail grinding, as shown in Figure 8a, it can be seen that the amplitude of the inner rail surface irregularity is significantly larger than that of the outer rail. The amplitude of the inner rail surface irregularity is between 250 μm~200 μm, the amplitude of the outer rail surface irregularity is less than 40 μm, and the inner rail surface irregularity presents a wavy shape with a wavelength of 30 mm, which is consistent with the field photo shown in Figure 1. After rail grinding, as shown in Figure 8b, there is no obvious periodicity that appears on the rail surface, this therefore means that rail grinding eliminates the corrugation.

Next, we use the EU standard (EN: ISO 3095: 2005(E)) to conduct a spectral analysis of rail surface irregularity for the entire measurement section [27], the rail surface irregularity level was then measured and compared to the ISO 3095 level standard. Both the measurement and comparison are shown in Figure 9.

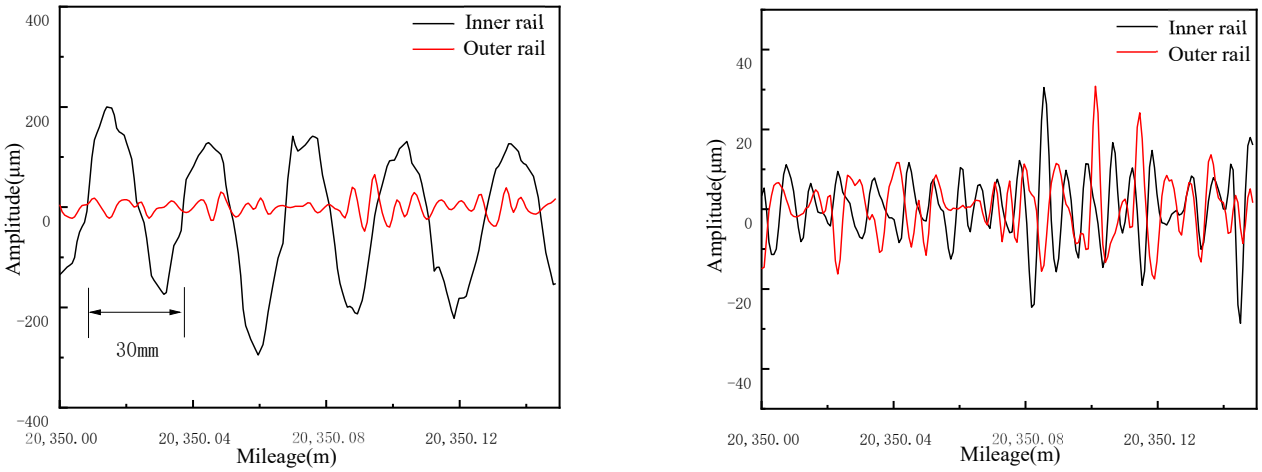

Figure 8. The amplitude of rail surface irregularity: (**a**) before rail grinding; (**b**) after rail grinding.

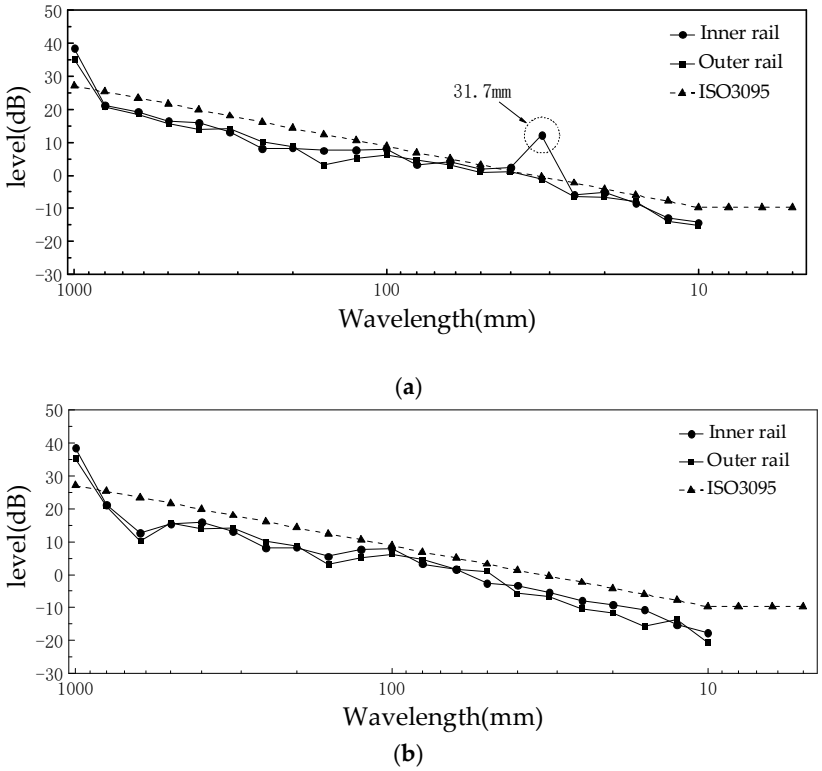

Figure 9. One-third octave analysis results of rail surface irregularity: (**a**) before rail grinding; (**b**) after rail grinding.

As can be seen from Figure 9a, the inner rail and outer rail surface irregularity are measured at 1000 mm. The inner rail at a wavelength of 31.7 mm amplitude level exceeds the ISO3095: 2005 standard reference value; other wavelength ranges do not exceed the ISO3095: 2005 standard reference value. The peak value of the inner rail surface irregularity level at a wavelength of 31.7 mm indicates the presence of a short-pitch rail corrugation; however, the outer rail does not show corrugation. After rail grinding, as shown in Figure 9b, there is no obvious peak value appearing on the rail surface irregularity level, this therefore means that rail grinding eliminates the corrugation.

The field-measured train running speed is 50 km/h and the wavelength of rail corrugation is 31.7 mm. The train passing frequency f on the corrugated rail can be obtained by Equation (4):

$$f = \frac{v}{\lambda} \tag{4}$$

where v is the train running speed, and λ is the rail corrugation wavelength.

From the calculation of Equation (4), it can be shown that the passing frequency of the train on the corrugated rail is approximately 438 Hz.

After rail grinding, the vertical vibration acceleration of the inner and outer rails is shown in Figure 10a,b. Through a Fourier transformation of the acceleration time-domain data, the rails' vertical, vibration, acceleration power spectral density is shown in Figure 10c,d.

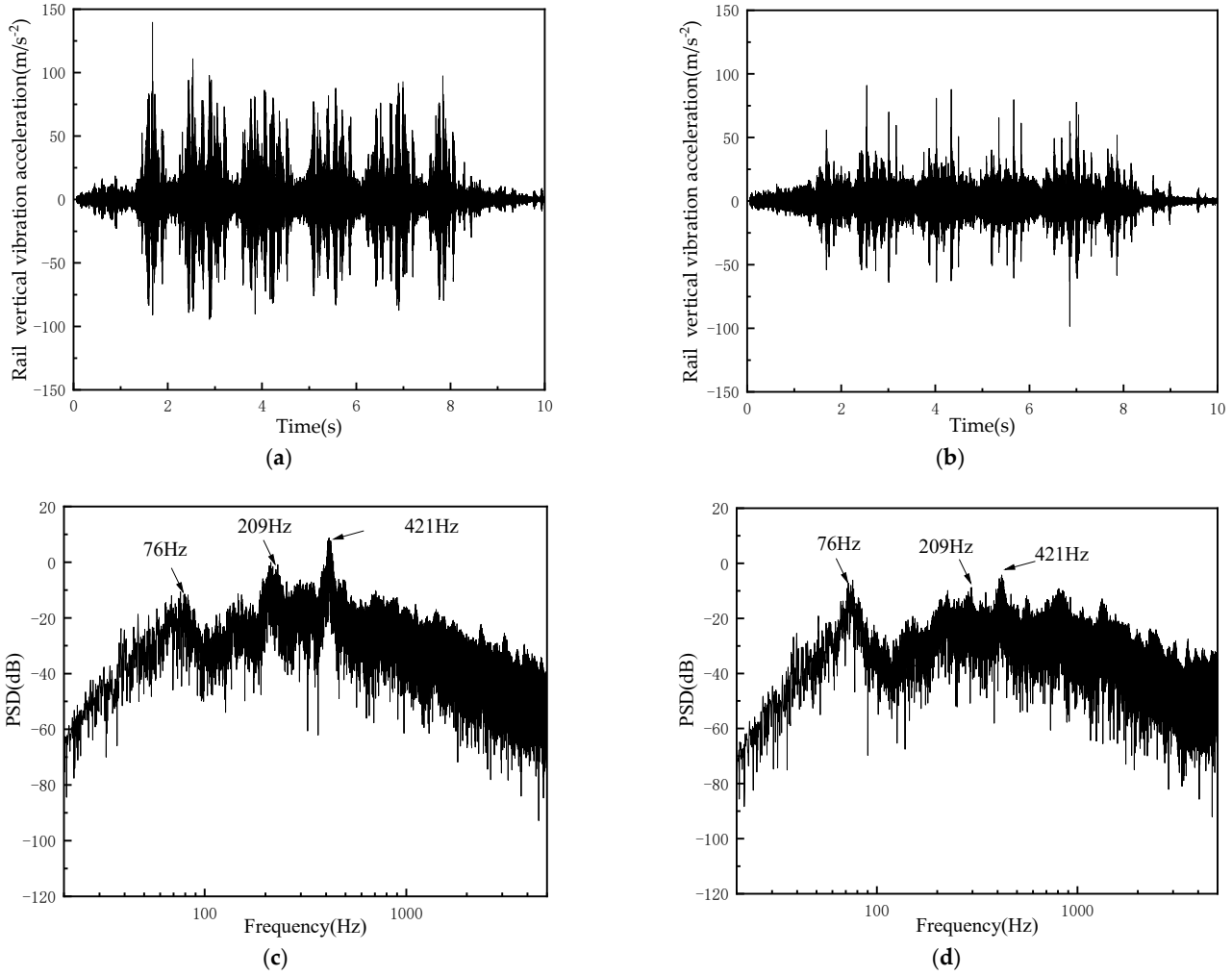

Figure 10. Measured data of the vertical, vibration acceleration on the rail: (**a**) acceleration data of inner rail; (**b**) acceleration data of outer rail; (**c**) PSD of acceleration data of inner rail; (**d**) PSD of acceleration data of inner rail.

Figure 10a,b shows the measured time-domain data of vertical, vibration, acceleration of the inner and outer rail when a train travels across the mounting position of sensors. It was found that the oscillation amplitude of vibration acceleration on the rail surface has significant fluctuations when the wheelsets pass through the measuring points. The vibration amplitude of the vertical vibration acceleration of the inner rail is larger than that of the outer rail. Figure 10c,d show a power density spectrum. It was found that there are several dominant frequencies in the vertical, vibration acceleration of the inner rail and

outer rail, which are 76 Hz, 209 Hz, and 421 Hz, respectively. The maximum power spectral density occurs at 421 Hz, and the inner rail power spectral density is significantly greater than the outer rail power spectral density.

Since the rail vibration acceleration is measured after the rail corrugation grinding, there is no corrugation excitation. Therefore, the vibration—with the frequency of 421 Hz—which appeared in the inner rail, is the frictional, self-excited vibration, which is similar to the corrugation passing frequency before rail grinding.

4.2. Results of the Complex Eigenvalue Analysis

The effective damping ratio is an important parameter for measuring the tendency of a self-excited vibration occurrence. When the effective damping ratio is negative, this indicates that system (1) is unstable [25], and that frictional, self-excited vibration may occur. The unstable vibration frequencies of the system are listed in Table 2, via complex eigenvalue analysis [25]. Distribution of the negative effective damping ratios of the system is given in Figure 11, where the unstable vibration frequency of 425.7 Hz corresponds to an effective damping ratio of −0.0115; further, the unstable vibration frequency of less than 1165.9 Hz corresponds to an effective damping ratio of −0.00134.

Table 2. System Unstable Frequency Distribution.

Complex Modals Order	Frequency
116	425.7
319	1165.9

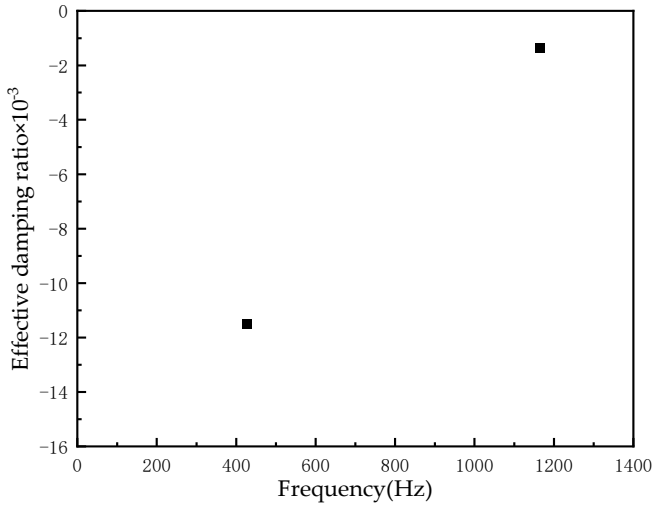

Figure 11. Distribution of the effective damping ratios of the wheelset-SSFST system.

The corresponding vibration patterns of unstable frequencies are shown in Figure 12. As can be seen in Figure 12a,b, unstable vibrations of the system mainly occur on the inner wheel and the inner rail.

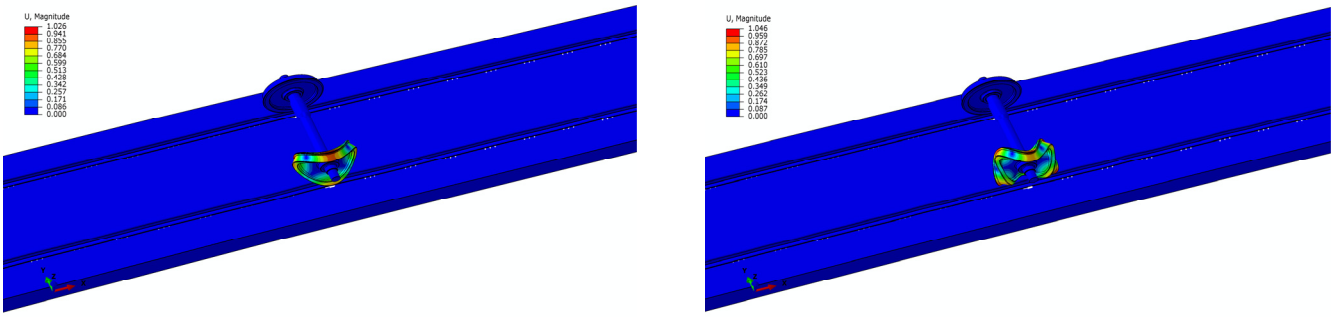

(**a**) (**b**)

Figure 12. Patterns of Unstable Modes of System: (**a**) f = 425.7 Hz and (**b**) f = 1165.9 Hz.

4.3. Results of Transit Analysis

Using Equation (3) for step-by-step integration, the results at the middle point of the curved track are extracted to obtain the inner rail and outer rail surface vertical vibration acceleration, as shown in Figure 13, and to also obtain the normal contact force data of the inner wheel–inner rail and outer wheel–outer rail, as shown in Figure 14.

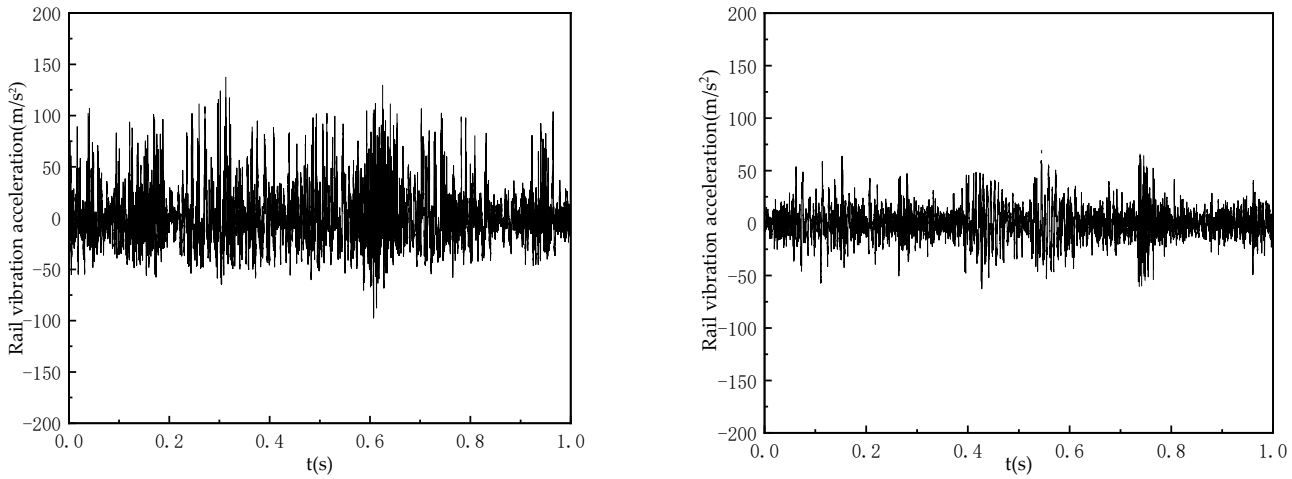

(**a**) (**b**)

Figure 13. Simulated vibration acceleration of the rail surface: (**a**) inner rail; (**b**) outer rail.

From Figure 13, it can be seen that when the wheelset passes through the SSFST section, the rail surface vibration acceleration on the inner rail is significantly larger than the rail surface vertical vibration acceleration on the outer rail, which indicates that the inner rail has a strong frictional, self-excited vibration.

According to the simulation results in Figure 14a,b, it was found that when the frictional, self-excited vibration occurs in the wheelset-SSFST system, the normal contact force of the inner rail is also significantly larger than that of the outer rail. It can also be seen from Figure 14c that the dominant frequency of the normal force of the inner rail contact is 422 Hz, which is less than a 3.6% deviation from the frequency of the first unstable vibration mode. As shown in Figure 14d, it is also found that there are three dominant frequencies of 415 Hz in the vertical vibration acceleration of the outer rail.

It can be inferred from Equation (3) that the w also changes according to the frequency of frictional, self-excited vibration. Therefore, periodic wear will occur on a rail surface with the same frequency of frictional, self-excited vibration. That is to say, frictional, self-excited vibration occurring on the inner rail is the reason for rail corrugation in the SSFST section, which is nearly consistent with the conclusion that the inner rail corrugation passing frequency, found in the field measurement, is 438 Hz.

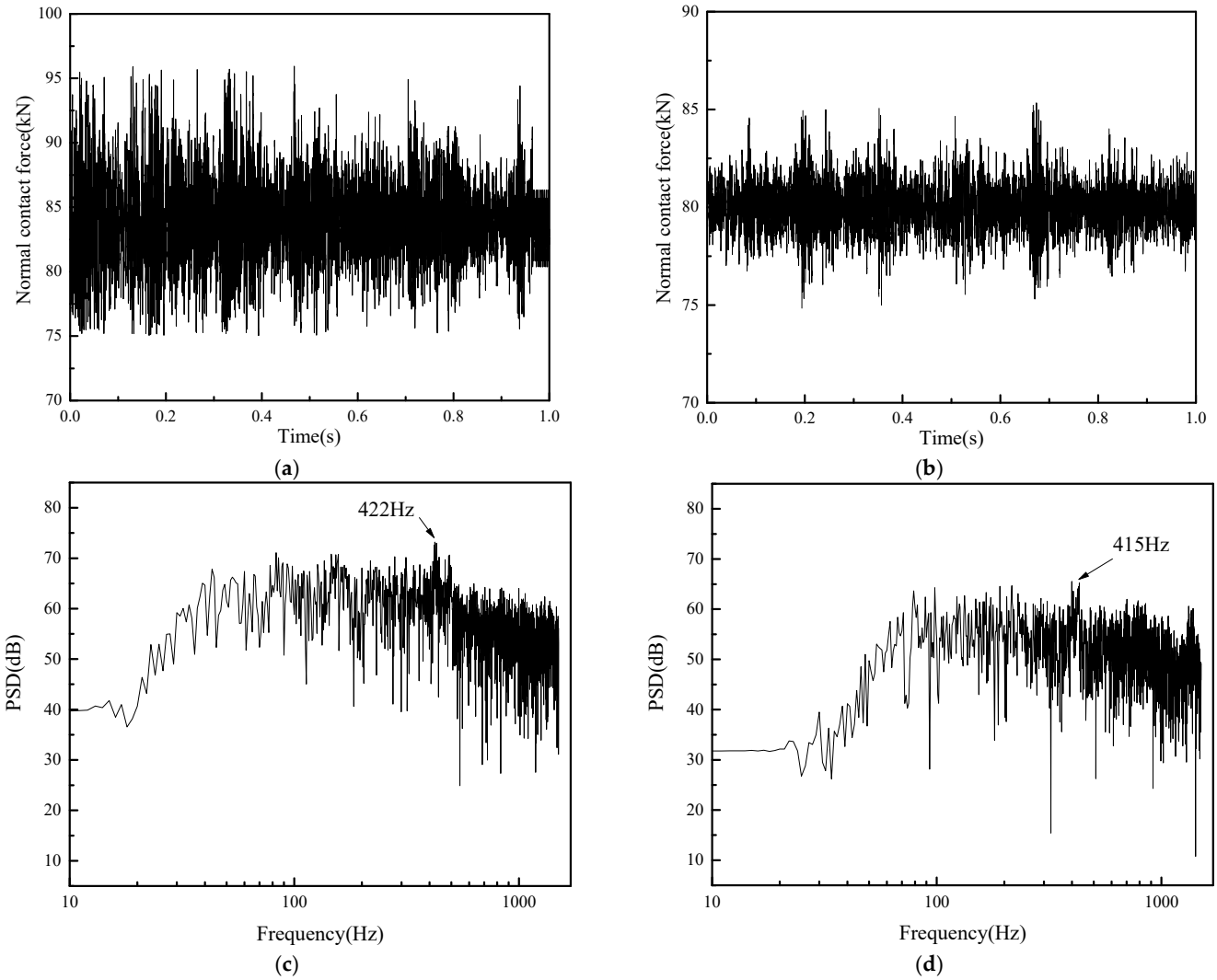

Figure 14. Simulated wheel–rail normal contact force: (**a**) normal contact force on the inner rail; (**b**) normal contact force on the outer rail; (**c**) PSD (Power spectral density) of normal contact force on the inner rail; (**d**) PSD of normal contact force on the outer rail.

5. The Effect of Model Parameter on Rail Corrugation

Wheelset-SSFST system structural parameters, such as fastener stiffness, steel spring stiffness, and the wheel–rail friction coefficient, have a direct effect on rail corrugation. Based on the frictional, self-excited vibration theory, the larger the absolute value of the negative effective damping ratios, the more likely it is for frictional, self-excited vibration to occur in the system [28], leading to the appearance of rail corrugation. Therefore, to achieve an in-depth analysis of the influence of these parameters on rail corrugation, this paper sets different parameter conditions. Notably, through a complex eigenvalue analysis that is obtained by the absolute value of the negative effective damping ratios, as an indicator for parameter impact analysis.

5.1. The Fastener Stiffness Influence Analysis

Fastener vertical stiffness was observed in the range of 20~60 kN/mm and lateral stiffness in the 5~10 kN/mm range. We set the fastener stiffness cases, as shown in Table 3, to be based on the established model for complex eigenvalue analysis in order to obtain the frequency and absolute value of the negative effective damping ratios, as shown in Figure 15.

Table 3. Fastener Stiffness cases (in KN/mm).

Case	1	2	3	4	5	6	7	8	9
Vertical stiffness	20	20	20	40	40	40	60	60	60
Lateral stiffness	5	8.79	10	5	8.79	10	5	8.79	10

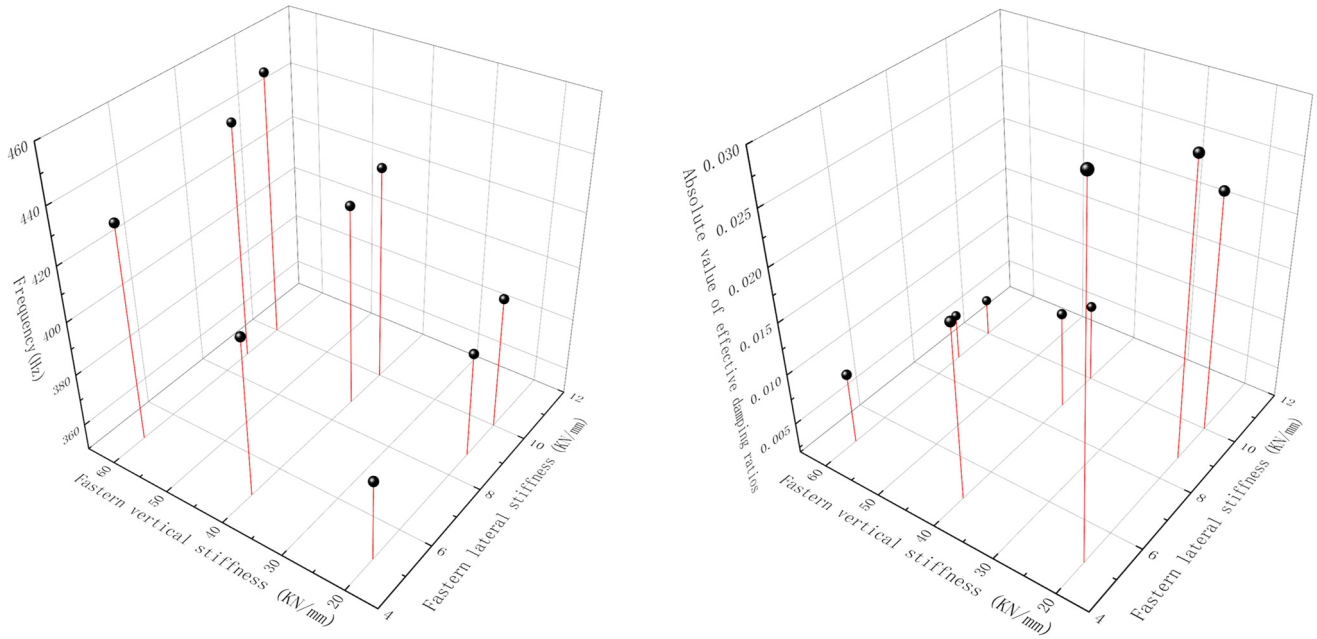

(**a**) (**b**)

Figure 15. Complex eigenvalue analysis results of different fasteners' stiffness cases: (**a**) frequency; (**b**) absolute value of effective damping ratios.

From Figure 15, it can be seen that the absolute value of the negative effective damping ratios of the wheelset-SSFST system will show a decreasing trend with an increase in fastener vertical and lateral stiffness. The corresponding frequency also increases, indicating that the smaller the fastener's vertical and lateral stiffness is, then the greater the probability of self-excited vibration. Therefore, the appropriate increase in the fastener's vertical and lateral stiffness will slow down the trend of rail corrugation and make the rail corrugation's wavelength smaller.

5.2. The Steel Spring Stiffness Influence Analysis

The steel spring stiffness values were selected at 5.3 kN/mm and 6.6 kN/mm, which are values commonly used on the metro, and the steel springs' lateral stiffness were selected as varying within the range from 6 to 10 kN/mm. The steel springs' stiffness cases were set as shown in Table 4, and a complex eigenvalue analysis was carried out based on the established model to obtain the frequency and absolute value of the negative effective damping ratios, as shown in Figure 16.

Table 4. Steel Spring Stiffness cases (in KN/mm).

Case	1	2	3	4	5	6
Vertical stiffness	5.3	5.3	5.3	6.6	6.6	6.6
Lateral stiffness	6	8	10	6	8	10

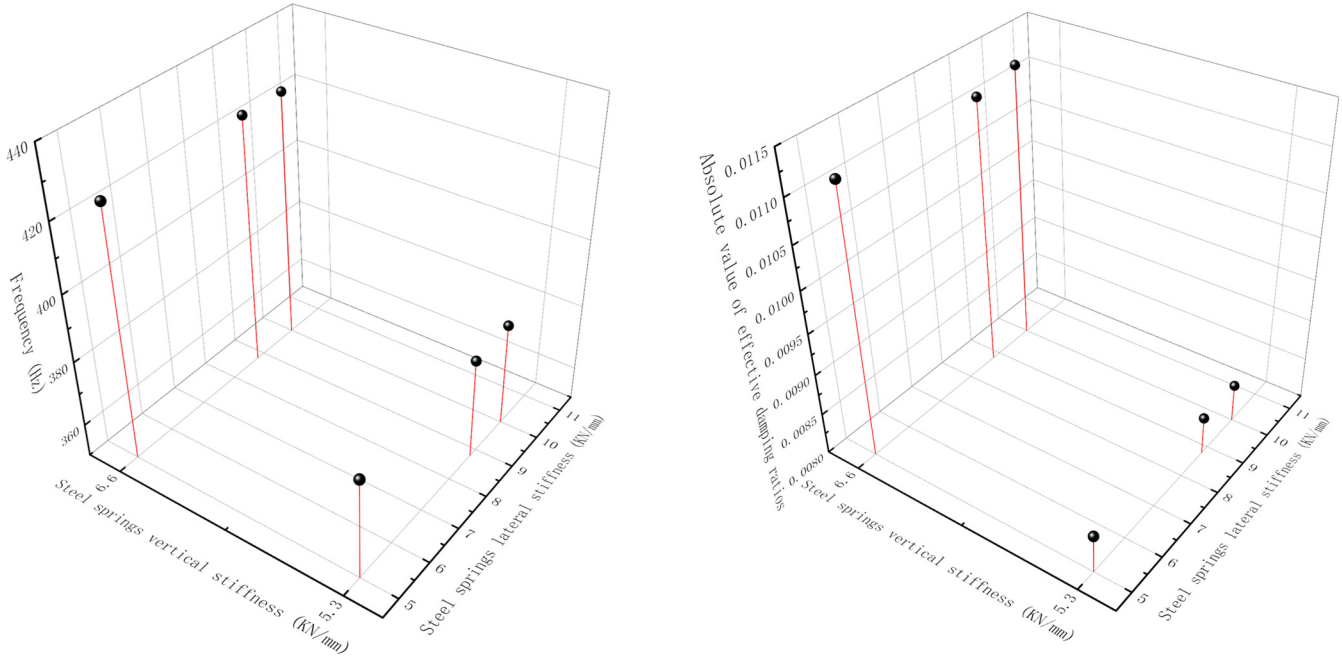

(**a**) (**b**)

Figure 16. Complex eigenvalue analysis results of different isolators stiffness cases: (**a**) frequency; (**b**) absolute value of effective damping ratios.

The results of different cases are shown in Figure 16. It can be seen that the absolute value of the negative effective damping ratios of the wheelset-SSFST system will increase with the steel springs' vertical stiffness, therefore showing a decreasing trend and corresponding to an increasing trend in frequency. With the steel springs' lateral stiffness increase, the effective damping ratios almost do not change. Therefore, increasing the steel springs' vertical stiffness can suppress self-excited vibration, which will also lead to an increase in the self-excited vibration frequency, thereby suppressing rail corrugation and reducing the rail corrugation wavelength. However, adjusting the steel springs' lateral stiffness cannot play a role in slowing down rail corrugation.

5.3. Analysis of the Influence of Friction Coefficient

The friction coefficient between wheel–rail interfaces is related to temperature, microscopic roughness, lubrication, and other factors that have an important influence on wheel–rail interactions. During operation, the friction coefficient decreases to 0.2 in the case of lubrication and increases to 0.6 on the wheel–rail surface in the case of sanding treatment [29]. Therefore, in this paper, by setting the friction coefficient to 0.2, 0.3, 0.4, 0.5, and 0.6 for the five conditions, for system complex eigenvalue analysis, the frequency and absolute value-effective damping ratio calculation results are shown in Figure 17.

Figure 17a,b show the frequency and maximum absolute value of effective damping ratios of the system under different friction coefficients. From Figure 17, it can be seen that the larger the friction coefficient, the greater the possibility of frictional, self-excited vibration in the wheelset-SSFST system, and the higher the frequency of frictional, self-excited vibration. Therefore, the possibility of rail corrugation in the wheel-SSFST system will increase along with the increase in the friction coefficient on the wheelset-SSFST surface. The rail corrugation wavelength will also decrease with the increase in the friction coefficient.

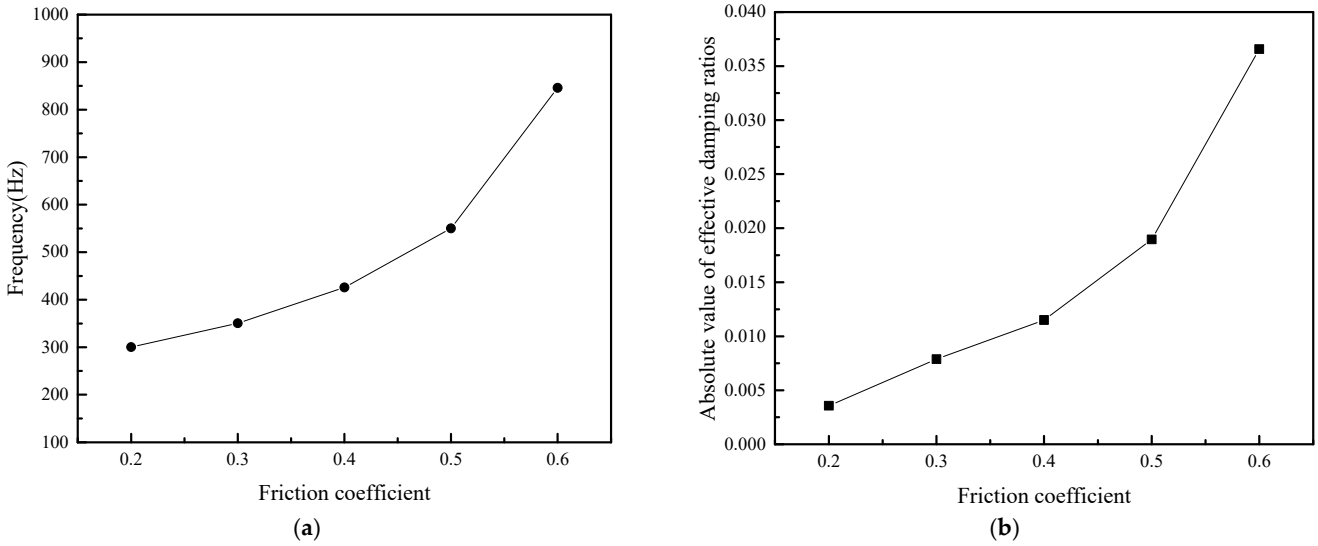

Figure 17. Complex eigenvalue analysis results in different cases of friction coefficients: (**a**) frequency; (**b**) absolute value of effective damping ratios.

6. Conclusions

Through onsite rail corrugation measurement of an SSFST section and the establishment of a wheelset-SSFST three-dimensional finite element model based on the onsite working conditions, complex eigenvalue and transient analyses were conducted. The aim was to study the frictional, self-excited vibration characteristics of the wheelset-SSFST coupling system. The following conclusions were obtained.

(1) The field rail corrugation measurement results show that rail corrugation in the SSFST section mainly occurs on the inner rail with a wavelength of approximately 31.7 mm, and the passing frequency of the train in the rail corrugation section is approximately 438 Hz. Through the PSD of rail vibration, acceleration was measured after the rail corrugation grinding. It was found that the vibration with a frequency of 421 Hz appearing in the inner rail is a frictional, self-excited vibration, which is similar to the corrugation passing frequency before rail grinding.

(2) The complex eigenvalue analysis shows that the frequency of the frictional, self-excited instability mode is 425.7 Hz, as well as 1165.9 Hz, and through the transient analysis, it is found that the rail surface, vibration acceleration on the inner rail is significantly larger than the rail surface vertical vibration acceleration on the outer rail. The main frequency of normal contact force on the inner rail is 415 Hz, which proves that the vibration corresponding to the first unstable vibration mode occurs in the wheelset-SSFST system and is also nearly consistent with the rail corrugation site passing frequency of 438 Hz. Therefore, the frictional, self-excited vibration caused by the creep force between the wheel and rail is the cause for the occurrence of rail corrugation in the inner rail of SSFST.

(3) Through parametric analysis of the model, it was found that the increase in the fastener's vertical and lateral stiffness leads to a decrease in the possibility of the occurrence of rail corrugation. The increase in the steel springs' vertical stiffness will cause the likelihood of the occurrence of rail corrugation to decrease, while the steel springs' lateral stiffness has little effect on rail corrugation. The increase in the friction coefficient will lead to a sharp increase in the tendency of the occurrence of rail corrugation and will cause the rail corrugation wavelength to decrease.

Funding: This research was funded by the National Natural Science Foundation of China (No. 52178436, 51778484).

Data Availability Statement: The data that support the findings of this study are available from the corresponding author upon reasonable request.

Acknowledgments: The authors gratefully acknowledge the Research Funds of Suzhou Rail Transit Group Co., Ltd., Suzhou, China.

Conflicts of Interest: The authors declare no conflict of interest.

References

1. Sato, Y.; Matsumoto, A.; Knothe, K. Review on rail corrugation studies. *Wear* **2002**, *253*, 130–139. [CrossRef]
2. Zhao, X.; Wen, Z.; Wang, F.; Jin, X.; Zhu, M. Modeling of high-speed wheel-rail rolling contact on a corrugated rail and corrugation development. *J. Zhejiang Univ.-Sci. A* **2014**, *15*, 946–963. [CrossRef]
3. Grassie, S.L. Rail corrugation: Advances in measurement, understanding and treatment. *Wear* **2005**, *258*, 1224–1234. [CrossRef]
4. Tuz, L.; Ziewiec, A.; Pańcikiewicz, K. Influence of the Thermal Cutting Process on Cracking of Pearlitic Steels. *Materials* **2021**, *14*, 1284. [CrossRef] [PubMed]
5. Mesaritis, M.; Shamsa, M.; Cuervo, P.; Santa, J.F.; Toro, A.; Marshall, M.B.; Lewis, R. A laboratory demonstration of rail grinding and analysis of running roughness and wear. *Wear* **2020**, *456–457*, 203379. [CrossRef]
6. Haarmann, A. *Die Baustoffe der Spurbahnen: Stahl and Eisen 1*; Kisling: Berlin, Germany, 1913; pp. 1–12. (In German)
7. Grassie, S.L. *Wheel-Rail Interface Handbook*; Woodhead Publishing: Cambridge, UK, 2009; pp. 349–376.
8. Grassie, S.L. Rail corrugation: Characteristics, causes, and treatments. *Proc. Inst. Mech. Eng. Part F J. Rail Rapid Transit* **2009**, *223*, 581–596. [CrossRef]
9. Matsumoto, A.; Sato, Y.; Ono, H.; Tanimoto, M.; Oka, Y.; Miyauchi, E. Formation mechanism and countermeasures of rail corrugation on curved track. *Wear* **2002**, *253*, 178–184. [CrossRef]
10. Sun, Y.Q.; Simson, S. Nonlinear three-dimensional wagon-track model for the investigation of rail corrugation initiation on curved track. *Veh. Syst. Dyn.* **2007**, *45*, 113–132. [CrossRef]
11. Ostermeijer, K.H. Review on short pitch rail corrugation studies. *Wear* **2008**, *265*, 1231–1237. [CrossRef]
12. Ma, C.; Gao, L.; Xin, T.; Cai, X.; Nadakatti, M.M.; Wang, P. The dynamic resonance under multiple flexible wheelset-rail interactions and its influence on rail corrugation for high-speed railway. *J. Sound Vib.* **2021**, *1*, 115968. [CrossRef]
13. Meehan, P.A.; Bellette, P.A.; Horwood, R.J. "Does god play dice with corrugations?": Environmental effects on growth. *Wear* **2014**, *314*, 254–260. [CrossRef]
14. Wu, T.X. Effects on short pitch rail corrugation growth of a rail vibration absorber/damper. *Wear* **2011**, *271*, 339–348. [CrossRef]
15. Li, W.; Wang, H.; Wen, Z.; Du, X.; Wu, L.; Li, X.; Jin, X. An investigation into the mechanism of metro rail corrugation using experimental and theoretical methods. *Proc. Inst. Mech. Eng. Part F J. Rail Rapid Transit* **2016**, *230*, 1025–1039. [CrossRef]
16. Cui, X.; Chen, G.; Yang, H.; Zhang, Q.; Ouyang, H.; Zhu, M. Study on rail corrugation of a metro tangential track with Cologne-egg type fasteners. *Veh. Syst. Dyn.* **2016**, *54*, 353–369. [CrossRef]
17. Wanming, Z.; Peng, X.U.; We, K. Analysis of vibration reduction characteristics and applicability of steel-spring floating-slab track. *J. Mod. Transp.* **2011**, *19*, 215–222.
18. Zhang, H.; Liu, W.; Liu, W.; Wu, Z. Study on the cause and treatment of rail corrugation for Beijing metro. *Wear* **2014**, *317*, 120–128. [CrossRef]
19. Xing, M.; Zhao, C.; Wang, P.; Lu, J.; Qiang, Y. A Numerical Analysis of Ground Vibration Induced by Typical Rail Corrugation of Underground Metro. *Shock. Vib.* **2019**, *2019*, 1–16.
20. Chen, G.X.; Zhou, Z.R.; Ouyang, H.; Jin, X.S.; Zhu, M.H.; Liu, Q.Y. A finite element study on rail corrugation based on saturated creep force-induced self-excited vibration of a wheelset-track system. *J. Sound Vib.* **2010**, *329*, 46–55. [CrossRef]
21. Xiong, Z.; Li, Q.; Mao, Q.; Zou, Q. A 3D Laser Profiling System for Rail Surface Defect Detection. *Sensors* **2017**, *17*, 1791. [CrossRef]
22. Yuan, Y. An eigenvalue analysis approach to brake squeal problem. In Proceedings of the 29th ISATA Conference, Florence, Italy, 1 January 1996.
23. Abubakar, A.R.; Ouyang, H. Complex eigenvalue analysis and dynamic transient in predicting disc brake squeal. *Veh. Noise Vib.* **2006**, *2*, 143–155. [CrossRef]
24. Hilber, H.M.; Hughes, T.J.R.; Taylor, R.L. Improved numerical dissipation for time integration algorithms in structural dynamics. *Earthq. Eng. Struct. Dyn.* **1977**, *5*, 283–292. [CrossRef]
25. Cui, X.; Chen, G.; Zhao, J.; Yan, W.; Ouyang, H.; Zhu, M. Field investigation and numerical study of the rail corrugation caused by frictional self-excited vibration. *Wear* **2017**, *376/377*, 1919–1929. [CrossRef]
26. Brockley, A. An investigation of rail corrugation using friction-induced vibration theory. *Wear* **1988**, *128*, 99–106. [CrossRef]
27. *BS EN ISO 3095: 2005*; Railway Applications—Acoustics—Measurement of Noise Emitted by Rail Bound Vehicles. BSI-British Standards Institution: London, UK, 2005.

28. Ibrahim, R.A. Friction-Induced Vibration, Chatter, Squeal, and Chaos—Part II: Dynamics and Modeling. *Appl. Mech. Rev.* **1994**, *47*, 227–253. [CrossRef]
29. Bucher, F.; Dmihrifv, A.I.; Ertz, M.; Knothe, K.; Popov, V.L.; Psakhie, S.G.; Shilko, E.V. Multiscale Simulation of Dry Friction in Wheel/Rail Contact. *Wear* **2006**, *261*, 87–88. [CrossRef]